

Bifurcations for counterintuitive post-inhibitory rebound spike related to absence epilepsy and Parkinson disease

Xian-Jun Wang(王宪军), Hua-Guang Gu(古华光), Yan-Bing Jia(贾雁兵), Bo Lu(陆博), and Hui Zhou(周辉)
Citation: Chin. Phys. B, 2023, 32 (**9**): 090502. DOI: 10.1088/1674-1056/acd7d3
Journal homepage: http://cpb.iphy.ac.cn; http://iopscience.iop.org/cpb

What follows is a list of articles you may be interested in

Synchronization-desynchronization transitions in networks of circle maps with sinusoidal coupling

Yun Zhai(翟云), Jinghua Xiao(肖井华), and Zhigang Zheng(郑志刚)
Chin. Phys. B, 2023, 32 (**6**): 060505. DOI: 10.1088/1674-1056/acc062

A novel fractional-order hyperchaotic complex system and its synchronization

Mengxin Jin(金孟鑫), Kehui Sun(孙克辉), and Shaobo He(贺少波)
Chin. Phys. B, 2023, 32 (**6**): 060501. DOI: 10.1088/1674-1056/acc0f6

Unstable periodic orbits analysis in the Qi system

Lian Jia(贾莲), Chengwei Dong(董成伟), Hantao Li(李瀚涛), and Xiaohong Sui(眭晓红)
Chin. Phys. B, 2023, 32 (**4**): 040502. DOI: 10.1088/1674-1056/aca9c3

Current bifurcation, reversals and multiple mobility transitions of dipole in alternating electric fields

Wei Du(杜威), Kao Jia(贾考), Zhi-Long Shi(施志龙), and Lin-Ru Nie(聂林如)
Chin. Phys. B, 2023, 32 (**2**): 020505. DOI: 10.1088/1674-1056/ac7dbe

Memristor hyperchaos in a generalized Kolmogorov-type system with extreme multistability

Xiaodong Jiao(焦晓东), Mingfeng Yuan(袁明峰), Jin Tao(陶金), Hao Sun(孙昊), Qinglin Sun(孙青林), and Zengqiang Chen(陈增强)
Chin. Phys. B, 2023, 32 (**1**): 010507. DOI: 10.1088/1674-1056/ac5e95

Bifurcations for counterintuitive post-inhibitory rebound spike related to absence epilepsy and Parkinson disease

Xian-Jun Wang(王宪军)[1], Hua-Guang Gu(古华光)[2,†], Yan-Bing Jia(贾雁兵)[3], Bo Lu(陆博)[1], and Hui Zhou(周辉)[1]

[1] *School of Mathematics and Science, Henan Institute of Science and Technology, Xinxiang* 453003, *China*
[2] *School of Aerospace Engineering and Applied Mechanics, Tongji University, Shanghai* 200092, *China*
[3] *School of Mathematics and Statistics, Henan University of Science and Technology, Luoyang* 471000, *China*

(Received 1 April 2023; revised manuscript received 25 April 2023; accepted manuscript online 23 May 2023)

Seizures are caused by increased neuronal firing activity resulting from reduced inhibitory effect and enhancement of inhibitory modulation to suppress this activity is used as a therapeutic tool. However, recent experiments have shown a counterintuitive phenomenon that inhibitory modulation does not suppress but elicit post-inhibitory rebound (PIR) spike along with seizure to challenge the therapeutic tool. The nonlinear mechanism to avoid the PIR spike can present theoretical guidance to seizure treatment. This paper focuses on identifying credible bifurcations that underlie PIR spike by modulating multiple parameters in multiple theoretical models. The study identifies a codimension-2 bifurcation called saddle–node homoclinic orbit ($SNHO_B$), which is an intersection between saddle node bifurcation on invariant cycle (SNIC) and other two bifurcations. PIR spike cannot be evoked for the SNIC far from the $SNHO_B$ but induced for the SNIC close to the $SNHO_B$, which extends the bifurcation condition for PIR spike from the well-known Hopf to SNIC. Especially, in a thalamic neuron model, increases of conductance of T-type Ca^{2+} (T_{Ca}) channel induce SNIC bifurcation approaching to the $SNHO_B$ to elicit PIR spikes, closely matching experimental results of the absence seizure or Parkinson diseases. Such results imply that, when inhibition is employed to relieve absence seizure and Parkinson diseases related to PIR spike, modulating SNIC to get far from the $SNHO_B$ to avoid PIR spike is the principle. The study also addresses the complex roles of T_{Ca} current and comprehensive relationships between PIR spike and nonlinear conceptions such as bifurcation types and shapes of threshold curve.

Keywords: bifurcation, threshold, post-inhibitory rebound spike, brain disease

PACS: 05.45.–a, 87.19.lg **DOI:** 10.1088/1674-1056/acd7d3

1. Introduction

Nonlinear physical concepts such as threshold and bifurcation are widely used in neuroscience to study the dynamics of firing behaviors in neurons.[1–8] These concepts play important roles in understanding brain functions and diseases, such as information coding, locomotion, and seizure.[9–15] The threshold is a basic conception to represent neuronal excitation property to external stimulation. Well known that a positive (or excitatory) stimulation beyond a threshold can elicit a spike, which has been widely accepted as common view. For some types of neurons, a negative (or inhibitory) stimulation stronger than one threshold can elicit spike as well, which presents paradoxical phenomenon different from the common view. To distinguish these two thresholds, the former is called "positive" threshold, whereas the latter is named "negative" threshold in the present paper. The spike induced by negative stimulation is known as post-inhibitory rebound (PIR) spike,[1,16–19] which is due to the existence of "negative" threshold. Such PIR spike is a paradoxical nonlinear phenomenon that differs from the suppression effect of inhibitory stimulation on firing activity. In neurophysiology, PIR spike is often mediated by special ionic currents such as low voltage-activated T-type calcium (T_{Ca}) current or hyperpolarization-activated cation current (Ih).[20–22] PIR phenomenon has been associated with multiple brain functions (such as memory, coding, and orienting[23–25]) and with many brain diseases (such as the Parkinson disease,[16,26] major depressive disease,[27,28] and seizure[29–32]). For example, in general, seizure is often paralleled with enhanced firing activity of excitatory pyramidal neuron induced by reduced inhibitory effect of inhibitory interneuron.[33–35] Therefore, enhancing the firing activity of interneurons to reduce the firing activity of pyramidal neurons is routinely employed as an anti-seizure strategy.[36–38] However, recent experiments have shown that enhanced inhibition of interneurons can induce PIR spikes of pyramidal neurons, presenting a novel etiology for seizure,[29–32] and challenging the traditional anti-seizure strategy.[36–38] Except for the PIR phenomenon, many investigations have shown many paradoxical phenomena that inhibitory modulation can induces spiking or bursting activity enhanced,[39–45] which are important for nonlinear science and neuroscience. Therefore, identifying the dynamical mechanism for the counterintuitive PIR phenomenon is crucial for recognizing brain functions and diseases.

[†]Corresponding author. E-mail: guhuaguang@tongji.edu.cn
© 2023 Chinese Physical Society and IOP Publishing Ltd

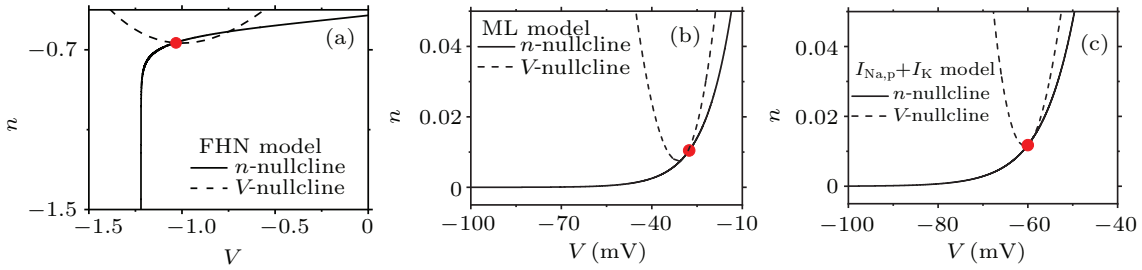


Fig. 1. The n-nullcline (solid curve), V-nullcline (dashed curve), and stable equilibrium point (red solid circle) for three different models. (a) FHN model. More details please refer to Ref. [46]; (b) ML model. $V_4 = 17.4$ mV and $I = 39.96$ μA/cm^2. Others please refer to Subsection 2.1; (c) $I_{Na,p} + I_K$ model. $k_n = 7$ mV and $I = 3.03$ μA/cm^2. Others please refer to Subsection 2.2.

In theory, PIR phenomenon has been related to threshold and bifurcation in multiple two-dimensional neuronal models composed of a variable of membrane potential (V) and a recovery variable (n).[1,18] In the well-known Morris–Lecar (ML) model, it has been widely accepted for a long time that PIR spike is not be caused for stable node near saddle-node bifurcation on an invariant circle (SNIC), which corresponds to "positive" threshold.[1] Instead, PIR spike can be induced from stable focus near Hopf bifurcation, which corresponds to the "negative" threshold.[1] Recently, PIR spike is built relationship to big homoclinic orbit (BHom) bifurcation with a special geometry (see Appendix A of the present paper or Ref. [18]). Moreover, PIR spike is simulated in Fitzhugh–Nagumo (FHN) model,[46] where the nearly vertical n-nullcline (solid black curve) left to the stable equilibrium point (red circle) is analytically approved to be a sufficient condition for PIR spike, as depicted in Fig. 1(a). Furthermore, seemingly contradictory with the well-known non-PIR spike for SNIC in the ML model,[1] PIR spike is induced for SNIC in the $I_{Na,p} + I_K$ model.[47] Different from FHN model, the n-nullcline left to the stable equilibrium point (red circle) in the ML and $I_{Na,p} + I_K$ models exhibits finite slope, as shown in Figs. 1(b) and 1(c), respectively. Inspired by the role of nearly infinite slope of n-nullcline played for PIR spike in FHN model,[46] one conjecture is that an increase in the slope of n-nullcline in the ML model may induce PIR spike or a decrease in slope of n-nullcline in the $I_{Na,p} + I_K$ model may induce non-PIR spike for the SNIC bifurcation, which is identified in the present paper.

The Hopf and SNIC bifurcations are widely accepted to correspond to types II and I excitability, respectively, and the codimension-2 bifurcation, Bogdanov–Takens (BT), is suggested to be the border between two types of excitability, and between two types of thresholds, and between PIR spike and non-PIR spike.[1,48,49] These theoretical results for PIR spike are mainly from theoretical models without Ih current or T_{Ca} current. Up to now, the dynamical mechanism for PIR spike mediated by T_{Ca} current remains unclearly. In some experiments,[16,26,29–32] PIR spikes observed in the thalamus neuron are mediated by T_{Ca} channel and are related to absence seizure or Parkinson diseases. For example, when applied inhibitory stimulation, thalamic neurons exhibit PIR spikes, which increases the incidence of absence seizure.[29] In addition, enhanced inhibitory stimulation from medial globus pallidus (GPm) neurons induces PIR spikes of thalamus neurons, promoting Parkinson disease-like tremor activity in muscles.[16] These results contradict the general viewpoint that inhibiting the firing activity of the thalamus is to ensure normal motor functions for healthy subjects.[50–54] These PIR spikes related to absence seizure and Parkinson diseases occur at large conductance of T_{Ca} channels, but not at small conductance, showing that the PIR spike is mediated by the T_{Ca} channel. The complex cooperations between two gates of T_{Ca} channel, one activation gate and the other inactivation gate, induces complex evolution of T_{Ca} current to underlie the PIR spikes.[55,56] Then, identification of dynamical mechanism for the PIR spike mediated by T_{Ca} channel and dynamics of T_{Ca} current are essential for understanding brain diseases such as absence seizure and Parkinson diseases.

This paper explores the relationship between post-inhibitory rebound (PIR) spikes, the threshold curves or surfaces, and bifurcations by modulating multiple parameters in multiple neuronal models, including a thalamic model. Firstly, our study acquires a universal bifurcation mechanism underlying PIR phenomena in four models, which all exhibit a codimension-2 bifurcation, called saddle-node homoclinic orbit (SNHO) bifurcation and labeled as SNHO_B in the present paper. Such SNHO_B is the intersection of SNIC, BHom, and saddle-node (SN) bifurcation, where subscript B denotes its relationship to BHom. PIR spike appears for the quiescent state near the SNIC close to the SNHO_B whereas not for the quiescent state near the SNIC far from the SNHO_B. Besides, the border between non-PIR spike and PIR spike occurs at a SNIC bifurcation close to the SNHO_B, instead of the previously suggested BT point. Secondly, the seeming contradiction between PIR spike in the $I_{Na,p} + I_K$ model and non-PIR spike in the ML model are well explained by the distances between SNIC and SNHO_B. The well-known SNIC for non-PIR spike in the ML model in Ref. [1] locates far from the SNHO_B. The SNIC for PIR spike in the $I_{Na,p} + I_K$ model in Ref. [47] is identified to be quite close to SNHO_B. For both models, with increasing the slope of n-nullcline, the SNIC gets closer to the SNHO_B and easier to elicit PIR spike. Finally, the SNHO_B

provides reasonable dynamical explanations for the inhibition-induced enhancement of firing behaviors in thalamus related to absence seizure or Parkinson diseases. With increasing the $T_{\rm Ca}$ current, the SNIC bifurcation changes to BHom via $\rm SNHO_B$. Neuronal electrical behaviors change from non-PIR spike to PIR spikes as SNIC bifurcation approaches to $\rm SNHO_B$. For a spiking behavior close to the $\rm SNHO_B$, inhibitory stimulation can induce silence at first and then enhanced spiking after inhibitory stimulation, labeled as PIR spiking. Both PIR spikes and spiking closely match the experimental results related to absence seizure or Parkinson diseases. Furthermore, complex dynamics of $T_{\rm Ca}$ current to mediate PIR phenomena are acquired to be related to the positive value and low threshold activation characteristics of $T_{\rm Ca}$ current. And the PIR spike or spiking is compared with the enhanced firing activity induced by inhibitory or positive stimulation. These results not only present bifurcation mechanism to the PIR spike and non-PIR spike, to the PIR phenomena mediated by $T_{\rm Ca}$ current, to the inhibition-induced firing enhancement related to brain diseases, but also provide theoretical guidance to the treatment of absence seizure and Parkinson diseases related to PIR spike, i.e., modulating SNIC to get far away from the $\rm SNHO_B$.

In the remaining parts of the present paper, Sections 2, 3, and 4 present the model and method, the main results, and the conclusions, respectively.

2. Model and methods

This section introduces the four neuronal models studied in the present paper.

2.1. ML model

The Morris–Lecar (ML) model is widely used to study firing activities related to SNIC bifurcation and Hopf bifurcation,[57] and reads as

$$C\frac{{\rm d}V}{{\rm d}t} = I + I_{\rm K} + I_{\rm Ca} + I_{\rm L}, \tag{1}$$

$$\frac{{\rm d}n}{{\rm d}t} = \frac{n_\infty(V) - n}{\gamma_n(V)}, \tag{2}$$

where V and n denote the membrane potential and gating variable of K^+ channel, respectively. C represents the membrane capacitance and I the depolarization current. $I_{\rm K} = -g_{\rm K} n (V - E_{\rm K})$, $I_{\rm Ca} = -g_{\rm Ca} m_\infty(V)(V - E_{\rm Ca})$, $I_{\rm L} = -g_{\rm L}(V - E_{\rm L})$ represent K^+, Ca^{2+}, and leakage currents. $E_{\rm K}$, $E_{\rm Ca}$, and $E_{\rm L}$ represent their reversal potentials, respectively. $g_{\rm K}$, $g_{\rm Ca}$, and $g_{\rm L}$ correspond to their maximal conductance, respectively. The functions

$$m_\infty(V) = \frac{1}{2}\left(1 + \tanh\frac{V - V_1}{V_2}\right),$$

$$n_\infty(V) = \frac{1}{2}\left(1 + \tanh\frac{V - V_3}{V_4}\right)$$

represent steady state of the gating variables, respectively, and

$$\gamma_n(V) = \left(0.067\cosh\frac{V - V_3}{2V_4}\right)^{-1}$$

denotes the voltage-dependent activation "time constant". The n-nullcline is described by $n = n_\infty(V)$ and its slope can be modulated by the parameter V_4 therein. The large V_4 value corresponds to the large slope of n-nullcline.

The parameter values read as follows: $C = 20$ μF/cm^2, $g_{\rm K} = 8$ μS/cm^2, $g_{\rm Ca} = 4$ μS/cm^2, $g_{\rm L} = 2$ μS/cm^2, $V_1 = -1.2$ mV, $V_2 = 18$ mV, $V_3 = 12$ mV, $E_{\rm K} = -84$ mV, $E_{\rm Ca} = 120$ mV, and $E_{\rm L} = -60$ mV. The control parameters are I with unit μA/cm^2 and V_4 with unit mV.

2.2. The $I_{\rm Na,p} + I_{\rm K}$ model

The $I_{\rm Na,p} + I_{\rm K}$ model[47] is another model widely used to study neural spiking activities, which reads as

$$C\frac{{\rm d}V}{{\rm d}t} = I + I_{\rm K} + I_{\rm Na,p} + I_{\rm L}, \tag{3}$$

$$\frac{{\rm d}n}{{\rm d}t} = \frac{n_\infty(V) - n}{\gamma_n(V)}, \tag{4}$$

where V and n respectively denotes the membrane potential and gating variable of K^+ channel. C and I have the same meanings as those of ML model. $I_{\rm K} = -g_{\rm K} n (V - E_{\rm K})$, $I_{\rm Na,p} = -g_{\rm Na} m_\infty(V)(V - E_{\rm Na})$, $I_{\rm L} = -g_{\rm L}(V - E_{\rm L})$ represent K^+, Na^+, and leakage currents. The Na^+ current is called persistent current due to slow inactivation characteristic. Their reversal potentials are denoted by $E_{\rm K}$, $E_{\rm Na}$, and $E_{\rm L}$, respectively. Their maximal conductances are denoted by $g_{\rm K}$, $g_{\rm Na}$, and $g_{\rm L}$, respectively. The functions

$$m_\infty(V) = \left(1 + \exp\left(\frac{V_{0.5,m} - V}{k_m}\right)\right)^{-1},$$

$$n_\infty(V) = \left(1 + \exp\left(\frac{V_{0.5,n} - V}{k_n}\right)\right)^{-1}$$

represent steady state of the gating variables, respectively, and $\gamma_n(V) = 1$ is for "time constant". The n-nullcline is described by $n = n_\infty(V)$ and its slope can be modulated by the parameter k_n therein. The increase in parameter k_n can increase the slope of n-nullcline.

The parameter values are read as follows: $C = 1$ μF/cm^2, $g_{\rm L} = 8$ μS/cm^2, $g_{\rm K} = 10$ μS/cm^2, $g_{\rm Na} = 20$ μS/cm^2, $V_{0.5,m} = -20$ mV, $V_{0.5,n} = -29$ mV, $k_m = 15$ mV, $E_{\rm L} = -79.42$ mV, $E_{\rm K} = -90$ mV, and $E_{\rm Na} = 60$ mV. The control parameters are I with unit μA/cm^2 and k_n with unit mV.

2.3. The $I_{\rm Na,p} + I_{\rm K}$ model with T-type Ca^{2+} current

A representative model for low voltage-activated T-type calcium ($T_{\rm Ca}$) current[58] is described as follows and labeled as $I_{\rm T}$

$$I_{\rm T} = -g_{\rm T} m_{\rm T,\infty}(V)\, h\,(V - E_{\rm T}), \tag{5}$$

$$\frac{\mathrm{d}h}{\mathrm{d}t}=\frac{h_\infty(V)-h}{\gamma_h(V)}, \tag{6}$$

where g_{T} denotes the conductance of T_{Ca} current and h the variable of inactivation gating. The functions

$$\gamma_h(V)=1.3\left(30+500\left(1+\exp\left(\frac{50+V}{3}\right)\right)^{-1}\right),$$
$$h_\infty(V)=\left(1+\exp\left(\frac{70+V}{4}\right)\right)^{-1}$$

represent the time constant and steady state of variable h, respectively. Notably, the variable h changes slowly due to the relatively large $\gamma_h(V)$. The steady state of activation gating variable of I_{T} current is denoted by

$$m_{\mathrm{T},\infty}(V)=\left(1+\exp\left(\frac{-40-V}{7.4}\right)\right)^{-1}.$$

The reversal potential $E_{\mathrm{T}}=90$ mV. Add I_{T} to right side of Eq. (3) and forms

$$C\frac{\mathrm{d}V}{\mathrm{d}t}=I+I_{\mathrm{K}}+I_{\mathrm{Na,p}}+I_{\mathrm{L}}+I_{\mathrm{T}}. \tag{7}$$

Then equations (4), (6), and (7) denote the $I_{\mathrm{Na,p}}+I_{\mathrm{K}}$ model with T_{Ca} current. The control parameters are I with units μA/cm^2 and g_{T} with units μS/cm^2. The parameter I can be adjusted by patch clamp and g_{T} can be modulated by application of blocker or agonist. The others in Eq. (7) are same with those in $I_{\mathrm{Na,p}}+I_{\mathrm{K}}$ model.

2.4. Thalamic model

Thalamic neurons are related to many brain functions or diseases such as sleep, absence seizure, and Parkinson diseases. A thalamic neuronal model which has been widely used to study Parkinson diseases is described as follows:[59]

$$C\frac{\mathrm{d}V}{\mathrm{d}t}=I+I_{\mathrm{K}}+I_{\mathrm{Na}}+I_{\mathrm{L}}+I_{\mathrm{T}}, \tag{8}$$
$$\frac{\mathrm{d}h_{\mathrm{Na}}}{\mathrm{d}t}=\frac{h_{\mathrm{Na},\infty}(V)-h_{\mathrm{Na}}}{\gamma_{h_{\mathrm{Na}}}(V)}, \tag{9}$$
$$\frac{\mathrm{d}h_{\mathrm{T}}}{\mathrm{d}t}=\frac{h_{\mathrm{T},\infty}(V)-h_{\mathrm{T}}}{\gamma_{h_{\mathrm{T}}}(V)}, \tag{10}$$

where V, h_{Na}, h_{T} denote membrane potential, inactivation gating variable of Na^+ channel, inactivation gating variable of T_{Ca} channel, respectively. $I_{\mathrm{K}}=-g_{\mathrm{K}}(0.75(1-h_{\mathrm{Na}}))^4(V-E_{\mathrm{K}})$, $I_{\mathrm{Na}}=-g_{\mathrm{Na}}m_\infty^3(V)h_{\mathrm{Na}}(V-E_{\mathrm{Na}})$, $I_{\mathrm{L}}=-g_{\mathrm{L}}(V-E_{\mathrm{L}})$, $I_{\mathrm{T}}=-g_{\mathrm{T}}p_{\mathrm{T},\infty}^2(V)h_{\mathrm{T}}(V-E_{\mathrm{T}})$ represent K^+, Na^+, leakage, T_{Ca} currents, respectively. The functions

$$m_\infty(V)=\left(1+\exp\left(\frac{-37-V}{7}\right)\right)^{-1},$$
$$h_{\mathrm{Na},\infty}(V)=\left(1+\exp\left(\frac{41+V}{4}\right)\right)^{-1},$$
$$\gamma_{h_{\mathrm{Na}}}(V)=\left(0.128\exp\left(\frac{-46-V}{18}\right)+4\left(1+\exp\left(\frac{-23-V}{5}\right)\right)^{-1}\right)^{-1},$$
$$h_{\mathrm{T},\infty}(V)=\left(1+\exp\left(\frac{84+V}{4}\right)\right)^{-1},$$
$$\gamma_{h_{\mathrm{T}}}(V)=28+\exp\left(\frac{-25-V}{10.5}\right).$$

Notably, the relatively large $\gamma_{h_{\mathrm{T}}}(V)$, which denotes the time constant of T_{Ca} current, results in a slowly changing variable h_{T}. The T_{Ca} current $I_{\mathrm{T}}=g_{\mathrm{T}}p_{\mathrm{T},\infty}^2(V)h_{\mathrm{T}}(V-E_{\mathrm{T}})$, where

$$p_{\mathrm{T},\infty}(V)=\left(1+\exp\left(\frac{-60-V}{6.2}\right)\right)^{-1}$$

denotes the steady state of the activation gating variable.

Other parameter values are as follows: $C=1$ μF/cm^2, $g_{\mathrm{L}}=0.05$ μS/cm^2, $g_{\mathrm{K}}=5$ μS/cm^2, $g_{\mathrm{Na}}=3$ μS/cm^2, $E_{\mathrm{L}}=-70$ mV, $E_{\mathrm{K}}=-90$ mV, $E_{\mathrm{Na}}=50$ mV, and $E_{\mathrm{T}}=0$ mV. The control parameters are I with units μA/cm^2 and g_{T} with units μS/cm^2.

2.5. Threshold curve or surface

The transient electrical behaviors of a resting neuron are dependent on the initial values in the phase plane or space. The whole phase plane or space is divided into two parts. One is called spike part, initiating from which neuronal electrical behavior forms action potential(s) before approaching the resting state. The other is called subthreshold part, initiating from which the phase trajectory does not form action potential but subthreshold oscillations. The border between these two parts forms the so-called threshold curve (two-dimensional system) or surface (three-dimensional system). Apparently, the stable equilibrium point (resting state) locates within the subthreshold part. If the inhibitory pulse stimulation pushes behaviors of such resting neuron beyond the threshold curve or surface (i.e., from subthreshold part to spike part), PIR spike is induced after the inhibitory stimulation, otherwise not.

2.6. Methods

In the present paper, a negative pulse stimulation is applied to a neuron to evoke PIR spike or spiking. Such pulse stimulation mimics the external direct current and/or synaptic current to evoke PIR spike in the biological experiment.

The bifurcation analysis is performed by Xppaut and Matcont.[60,61] The numerical integration is performed by fourth-order Runge–Kutta method with time step 0.01 ms.

3. Result

This section contains 5 subsections. Firstly, we study the relationships between the PIR spike, SNIC bifurcation, and

threshold curves in ML model (Subsection 3.1) and $I_{Na,p}+I_K$ model (Subsection 3.2) by changing the slope of n-nullcline. Secondly, the codiemsnion-2 bifurcation ($SNHO_B$) mechanism for PIR spike or not are acquired in ML model and $I_{Na,p}+I_K$ model (Subsection 3.3). The seemingly contradiction between the PIR spike in ML model and non-PIR spike in $I_{Na,p}+I_K$ model are well explained with the different distances of the SNIC to the $SNHO_B$. Finally, the codimension-2 bifurcation mechanism for PIR phenomena mediated by T_{Ca} current are acquired in $I_{Na,p}+I_K$ model with T_{Ca} current (Subsection 3.4) and thalamic model (Subsection 3.5). The inhibition-induced enhancement of firing behaviors is consistent with the results observed in experiments related to absence seizure and Parkinson diseases.

3.1. Increases in slope of n-nullcline induces non-PIR spike changed to PIR spike for ML model

The parameter V_4 in ML model can modulate the slope of n-nullcline. The large V_4 value corresponds to the large slope of n-nullcline. As V_4 increases from 17.4 mV, to 20 mV, and to 22.02 mV, the bifurcation type remains unchanged and belongs to SNIC, as depicted in top row of Fig. 2 (from left to right), respectively. The blue S-shaped curve is for the equilibriums and red curves denote the amplitude of stable limit cycle. The bottom, middle, and top branch of the S-shaped curve represent stable node, saddle, and unstable focus, respectively. The right knee of the S-shaped curve involves in the emerging stable limit cycle (red curves) and thus forms the SNIC bifurcation. The left knee denoted by SN_2 represents saddle-node (SN) bifurcation.

Shown in middle row of Fig. 2 is the inhibitory stimulation-induced response, whose initial state is set at the stable node (i.e., neuronal resting state) close to the SNIC bifurcation in top row. For $V_4 = 17.4$ mV and 20 mV, inhibitory stimulation (red, lower panel) with strong pulse strength $A = -200$ μA/cm^2 cannot induce PIR spike, as depicted in Figs. 2(a2) and 2(b2), respectively. The membrane potential (black, upper panel) firstly decreases during inhibitory stimulation, then recovers directly to the resting state after the stimulation. Such results are consistent with the common view of non-PIR spike in ML model in Ref. [1]. However, as V_4 increases to 22.02 mV, i.e., the slope of n-nullcline increases, PIR spike is evoked, as illustrated in Fig. 2(c2). After the inhibitory stimulation even with relatively weak pulse strength $A = -100$ μA/cm^2, an action potential (i.e., PIR spike) appears before recovering to the resting membrane potential. The PIR spike presents a novel result different from the previous view of non-PIR spike in ML model, which is further explained in Subsection 3.3.

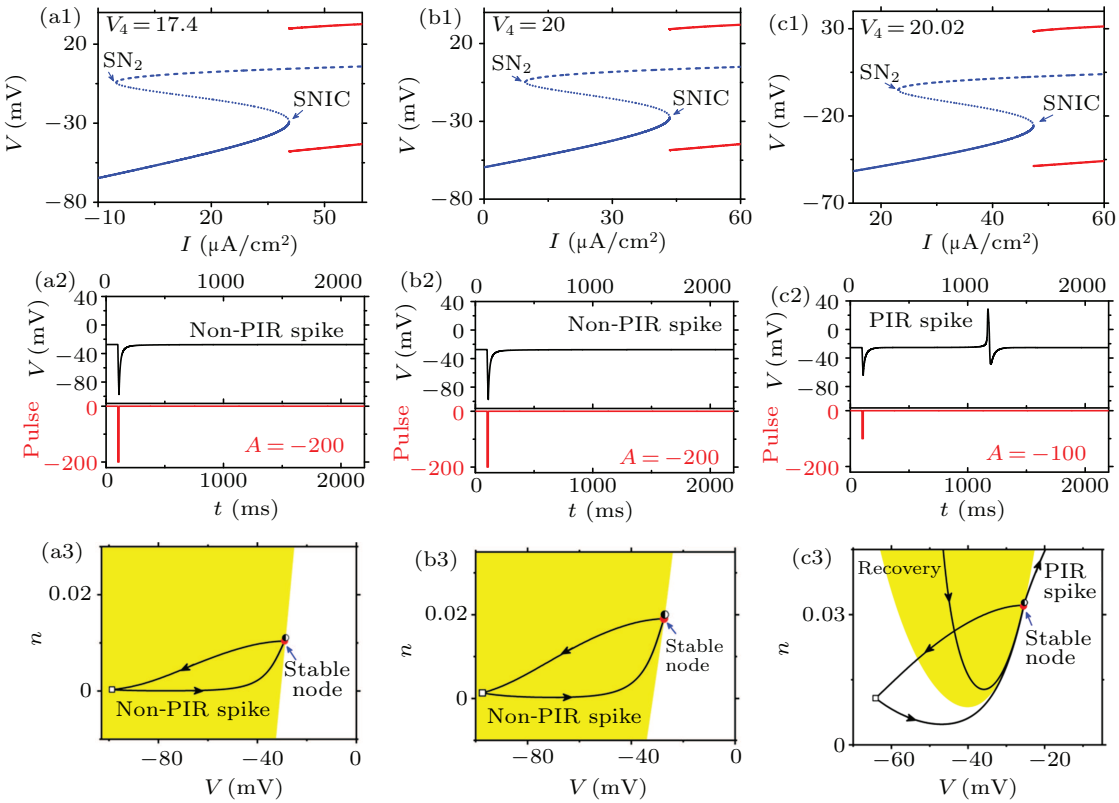


Fig. 2. Dynamics at different V_4 values in ML model. Top row: Bifurcation diagrams with respect to I. (a1) $V_4 = 17.4$ mV. SNIC occurs at $I \approx 39.96316$ μA/cm^2; (b1) $V_4 = 20$ mV. SNIC occurs at $I \approx 43.41065$ μA/cm^2; (c1) $V_4 = 22.02$ mV. SNIC occurs at $I \approx 47.37691$ μA/cm^2. Middle row: The response (black, upper panel) of node to inhibitory pulse stimulation (red, lower panel) with width 10 ms. (a2) Non-PIR spike. $V_4 = 17.4$ mV, $I = 39.963$ μA/cm^2, and pulse strength $A = 200$ μA/cm^2; (b2) Non-PIR spike. $V_4 = 20$ mV, $I = 43.410$ μA/cm^2, and $A = 200$ μA/cm^2; (c2) PIR spike. $V_4 = 22.02$ mV, $I = 47.376$ μA/cm^2, and $A = 100$ μA/cm^2. Bottom row: The threshold curve (i.e., the border between yellow and blank areas) for the PIR spike and non-PIR spike corresponding to the middle row. Red solid circle is for stable node, black half-filled circle for saddle, and hollow square for the termination of stimulation. The black arrow indicates the trajectory's running direction.

The geometrical change of threshold curves (i.e., border between blank and yellow areas) for above non-PIR spike and PIR spike are shown Figs. 2(a3), 2(b3), and 2(c3), respectively. Such threshold curve effectively distinguishes the dynamic behavior of the trajectory between action potential and subthreshold potential. Trajectories starting from a phase point in the blank region (the spike part) lead to an action potential, while those in the yellow region (the subthreshold part) do not. Shown in red circle is the stable node (resting state), which locates within the subthreshold part (yellow), and in half-filled circle is a saddle point, which locates on the threshold curve. These two points nearly coincide because they are very close to an SNIC bifurcation. The inhibitory stimulationevoked phase trajectory is represented by the black curve, where the square point denotes the termination of stimulation.

For smaller slope of n-nullcline, i.e., $V_4 = 17.4$ mV or $V_4 = 20$ mV, during inhibitory stimulation, V value decreased from the resting state (red circle) to square point, which locates within the yellow area, as shown in Figs. 2(a3) and 2(b3). After the stimulation, V increases and recovers to the resting state directly. All behaviors locate within the yellow area, then, no PIR spike is induced. The threshold curve exhibits higher V values than that of the resting state and corresponds to the "positive" threshold.

Different from smaller slope of n-nullcline ($V_4 = 17.4$ mV or 20 mV), the threshold curve for larger slope $V_4 = 20.02$ mV exhibits a part right to the resting state and a part left to the resting state, as shown in Fig. 2(c3). The right part of threshold curve exhibits V values larger than the resting state, corresponding to a "positive" threshold. The left part manifests V values smaller than the resting state, corresponding to a "negative" threshold. During the inhibitory stimulation, V decreases firstly, then passes through the "negative" threshold curve into blank area, and further decreases to the hollow square. After the stimulation, V increases to form the PIR spike, as illustrated in Fig. 2(c2), and then recovers to the resting state. Notably, it is the inhibitory stimulation-evoked trajectory running across the threshold curve that forms the PIR spike.

3.2. Decreases in slope of n-nullcline induces PIR spike changed to non-PIR spike in the $I_{\mathrm{Nap}} + I_{\mathrm{K}}$ model

In $I_{\mathrm{Na,p}} + I_{\mathrm{K}}$ model, the increase in parameter k_n can increase the slope of n-nullcline. The SNIC bifurcations at $k_n = 6$ mV, 6.5 mV, and 6.95 mV are depicted in Figs. 3(a1), 3(b1), and 3(c1), respectively. For SNIC at $k_n = 6.95$ mV (large slope), inhibitory stimulation with relatively weak strength ($A = -100$ μA/cm^2) evokes PIR spike, as depicted in Fig. 3(c2), similar to Ref. [47]. However, as k_n decreases to

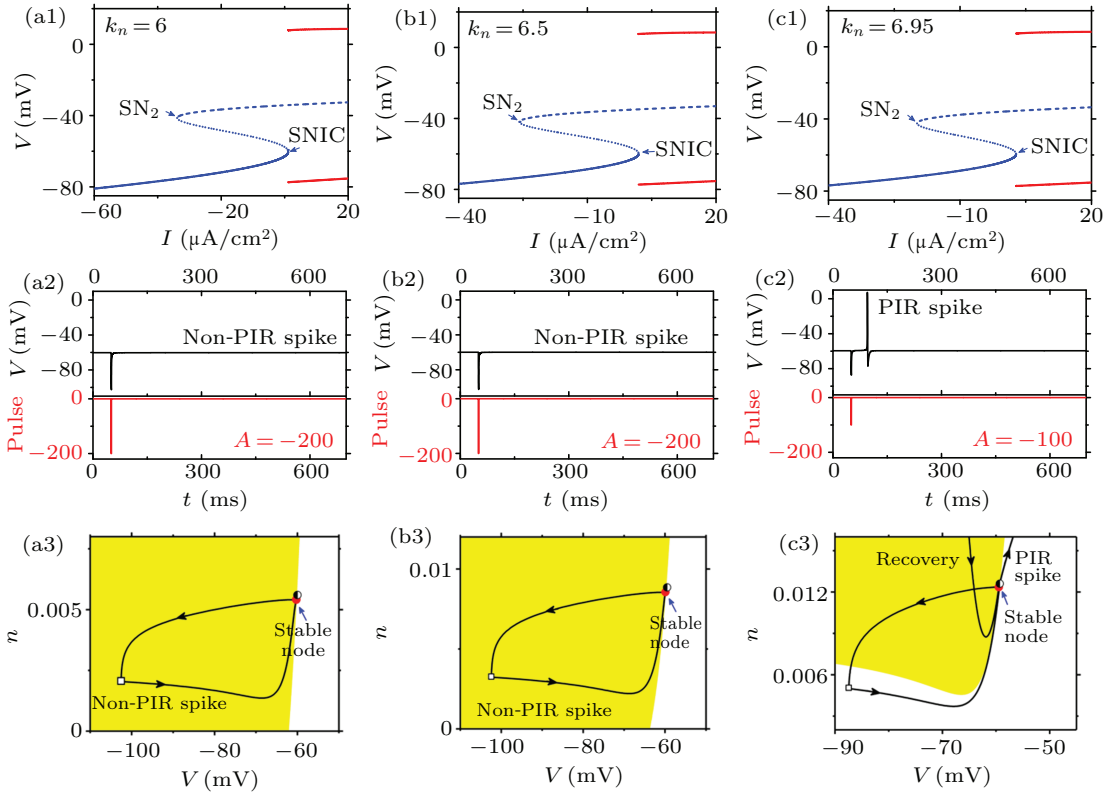


Fig. 3. Dynamics at different k_n values in $I_{\mathrm{Na,p}} + I_{\mathrm{K}}$ model. Top row: Bifurcation diagrams with increasing I. (a1) k_n =6 mV and SNIC occurs at $I \approx 1.145266$ μA/cm^2; (b1) $k_n = 6.5$ mV and SNIC occurs at $I \approx 1.962412$ μA/cm^2; (c1) $k_n = 6.95$ mV and SNIC occurs at $I \approx 2.916467$ μA/cm^2; Middle row: Response (upper) to inhibitory stimulation (lower) with pulse width 1 ms. (a2) Non-PIR spike, $k_n = 6$ mV, $I = 1.145$ μA/cm^2, and $A = 200$ μA/cm^2; (b2) Non-PIR spike. $k_n = 6.5$ mV, $I = 1.962$ μA/cm^2, and $A = 200$ μA/cm^2; (c2) PIR spike, $k_n = 6.95$ mV, $I = 2.916$ μA/cm^2, and $A = 100$ μA/cm^2. Bottom Row: The threshold curve (i.e., border between yellow and blank areas) for the PIR spike and non-PIR spike corresponding to middle row. Red solid circle is for stable node, black half-filled circle for saddle, and hollow square for the termination of stimulation. The black arrow indicates the trajectory's running direction. The color codes for yellow and blank areas please refer to Fig. 2.

6.5 mV and 6 mV (small slopes), even strong inhibitory stimulation ($A = -200$ μA/cm^2) cannot induce PIR spike, as depicted in Figs. 3(b2) and 3(a2). The initial resting states here are set at the stable node close to SNIC bifurcation in top row of Fig. 3, respectively. The changes of threshold curves with increasing k_n for $I_{\mathrm{Na,p}}+I_{\mathrm{K}}$ model resemble those with increasing V_4 of ML model, as shown in Figs. 3(a3), 3(b3), and 3(c3). Non-PIR spike for $k_n = 6$ mV and 6.5 mV corresponds to "positive" threshold (Figs. 3(a3), 3(b3)), and PIR spike for $k_n = 6.9$ mV corresponds to "negative" threshold (Fig. 3(c3)). The codes for the plots and colors here are same with those in Fig. 2 and thus the details are omitted to avoid redundancy.

3.3. PIR spike appears for SNIC close to SNHO$_{\mathrm{B}}$ in the ML and $I_{\mathrm{Na,p}}+I_{\mathrm{K}}$ model

Above results of PIR spike and non-PIR spike for SNIC bifurcations of ML model and $I_{\mathrm{Na,p}}+I_{\mathrm{K}}$ model can be explained with bifurcations in two-parameter plane, as depicted in Fig. 4, where left column is for ML model and right column for $I_{\mathrm{Na,p}}+I_{\mathrm{K}}$ model.

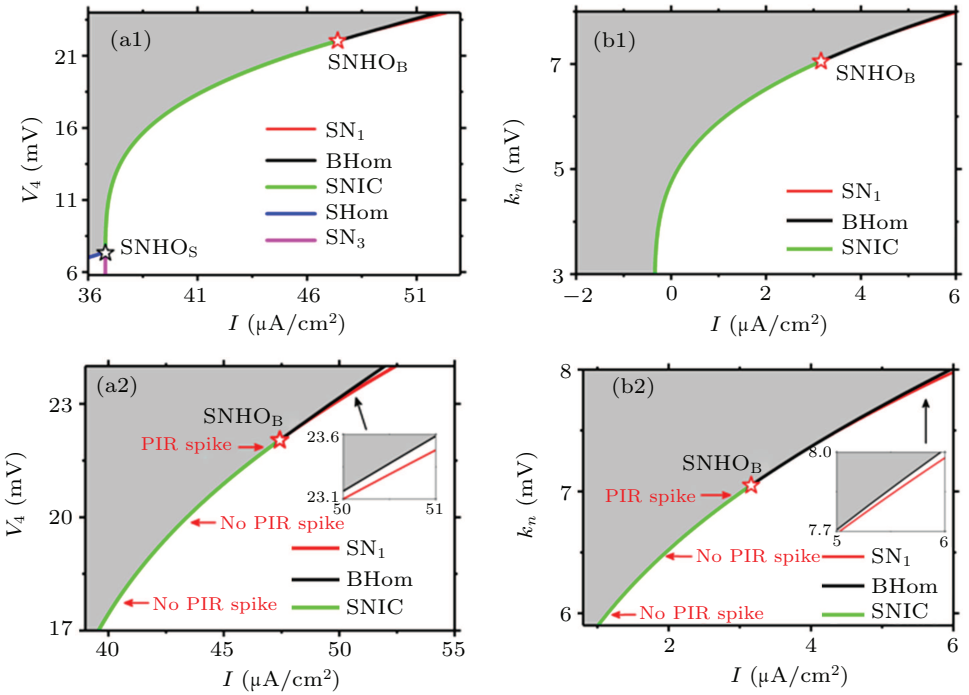


Fig. 4. Bifurcations in two-parameter plane. Green, blue, and black curves denote the SNIC, BHom, and SHom, respectively. Gray is for stable equilibrium and blank for stable limit cycle. In (I, V_4) plane of the ML model: (a1) codimension-2 bifurcation points SNHO$_{\mathrm{B}}$ (red star) and SNHO$_{\mathrm{S}}$ (black star); (a2) enlargement around SNHO$_{\mathrm{B}}$. The three horizontal arrows correspond to the three V_4 values in Fig. 2. In plane (I, k_n) of the $I_{\mathrm{Na,p}}+I_{\mathrm{K}}$ model: (b1) overall perspective of the bifurcations; (b2) enlargement around SNHO$_{\mathrm{B}}$. The three horizontal arrows correspond to the three k_n values in Fig. 3.

The bifurcations of ML model are shown in Fig. 4(a1) and its upper half plane is further enlarged in Fig. 4(a2). The bifurcation curve of SNIC (green) exists in a wide range, and the three examples of SNIC in Fig. 2 correspond to the red horizontal arrows in Fig. 4(a2). For large V_4, the red curve denotes the SN bifurcation (SN$_1$) and the black curve represents the BHom bifurcation. For small V_4, there exists another SN bifurcation curve (SN$_3$, magenta) and a small homoclinic bifurcation curve (SHom, blue). The focus of this paper is the SNIC bifurcation and its PIR spike. To not interrupt such focus, other bifurcations, such as the BHom, SHom, SN$_1$, SN$_3$, and the PIR spike for BHom and non-PIR spike for SHom, are thus shown in Appendix A. As illustrated in Fig. 4(a1), the SNIC, SN$_1$, and BHom bifurcation curves contact to form a codimension-2 bifurcation point, saddle-node homoclinic orbit bifurcation (SNHO), which is labeled as SNHO$_{\mathrm{B}}$ (red star), where the subscript "B" means that such SNHO bifurcation point is associated with BHom. The SNIC curve intersects with the SN$_3$ and SHom curves to form another SNHO, labeled as SNHO$_{\mathrm{S}}$ (black star), where the subscript "S" means that the SNHO is associated with SHom. Shown in gray is the mono-stable equilibrium point (resting neuron) and in blank the stable limit cycle (spiking neuron). Coexisting behaviors appear within the very narrow region between the black and red curves upper to the SNHO$_{\mathrm{B}}$.

The three horizontal arrows in Fig. 4(a2) correspond to three SNIC bifurcations in Fig. 2. The SNIC bifurcations at bottom two horizontal arrows ($V_4 = 17.4$ mV and 20 mV) correspond to non-PIR spike, and locate far from the SNHO$_{\mathrm{B}}$. To the contrary, the SNIC bifurcation with PIR spike at top horizontal arrow ($V_4 = 20.02$ mV) locates closely to the SNHO$_{\mathrm{B}}$. Therefore, one speculates that the PIR spike for SNIC appears when SNIC is close to the SNHO$_{\mathrm{B}}$, but does not when SNIC is far from the SNHO$_{\mathrm{B}}$. Furthermore, such a result suggests that border or the transition point between non-PIR spike and PIR spike occurs at certain SNIC bifurcation close to SNHO$_{\mathrm{B}}$.

However, one traditional viewpoint is that BT should underlie such border due to the wellknown PIR spike for Hopf bifurcation related to BT. Therefore, our results imply a novel transition point from non-PIR spike to PIR spike, which occurs at certain SNIC bifurcation close to $SNHO_B$ instead of BT. The BT bifurcation locates up-right to the $SNHO_B$ (not shown due to the excessively long distance between BT and $SNHO_B$).

Results around the $SNHO_B$ are further identified in $I_{Na,p}+I_K$ model, as illustrated in Figs. 4(b1) and 4(b2). Figure 4(b2) is the enlargement of the upper half part of Fig. 4(b1). For $I_{Na,p}+I_K$ model, except that there is no $SNHO_S$, the bifurcations are quite similar with those of ML model (Fig. 4(a1)). For example, the $SNHO_B$ (red star) also appears at the large slope of n-nullcline (i.e., large k_n). The three horizontal arrows in Fig. 4(b2) correspond to three k_n values of SNIC bifurcation in Fig. 3. The non-PIR spikes for SNIC bifurcations (at bottom two horizontal arrows with $k_n = 6$ mV and 6.5 mV) locate relatively far from the $SNHO_B$. The SNIC bifurcation for PIR spike (at top horizontal arrow with $k_n = 6.95$ mV) locates quite close to the $SNHO_B$. Besides, the SNIC for the PIR spike in $I_{Na,p}+I_K$ model in Ref. [47] occurs at $k_n = 7$ mV, which also locates quite close to the $SNHO_B$. These results further verify above speculation that PIR spike appears for the SNIC close to the $SNHO_B$ but not for the one far from the $SNHO_B$, which presents a novel viewpoint that the codimension-2 bifurcation point $SNHO_B$ plays a determinant role in modulation to the PIR spike. The PIR spike depends upon the distance between the SNIC bifurcation and $SNHO_B$. Such a result extends the conditions for the generation of PIR spike from codimension-1 bifurcation (such as Hopf and BHom) to codimension-2 bifurcation ($SNHO_B$).

In addition, PIR spike appears for the BHom, which is related to the $SNHO_B$ and shown in Appendix A. Besides, there is no PIR spike for the SHom, which is associated with the $SNHO_S$ and shown in Appendix A as well.

3.4. The relationship between $SNHO_B$ and PIR phenomenon in $I_{Na,p}+I_K$ model with T-type Ca^{2+} channel

Well known that T_{Ca} channel can mediate PIR phenomena in many neuronal systems. However, the bifurcation mechanism is still unclear up to now. Inspired by above results, the $SNHO_B$ is speculated to play such bifurcation mechanism for PIR phenomena mediated by T_{Ca} current, which is identified in this subsection and depicted in Fig. 5. In $I_{Na,p}+I_K$ model with T_{Ca} current, with increasing the strength of T_{Ca} (i.e., g_T), the SNIC bifurcation (green) changes to BHom (black) via $SNHO_B$ (red star). Meanwhile, the neuronal response to inhibitory stimulation changes from non-PIR spike to PIR spike as SNIC bifurcation (green) approaches the $SNHO_B$, as indicated by the red arrows in Fig. 5. The details are further depicted in Fig. 6.

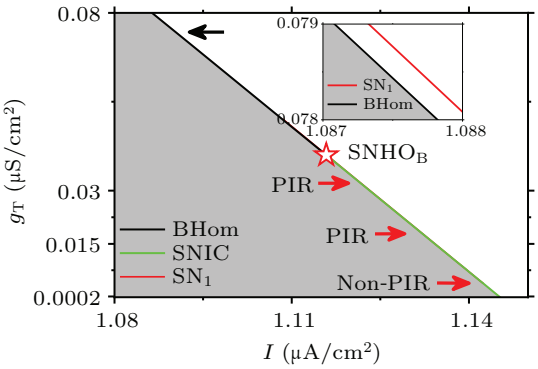


Fig. 5. The bifurcations in two-parameter plane (I, g_T) related to PIR spike and non-PIR spike in the $I_{Na,p}+I_K$ model with T_{Ca} current. The codes for plots and symbols and colors are same with those in Fig. 4. Inset shows the details at black arrow. The dynamics for the SNIC bifurcation at red arrows are shown in Fig. 6.

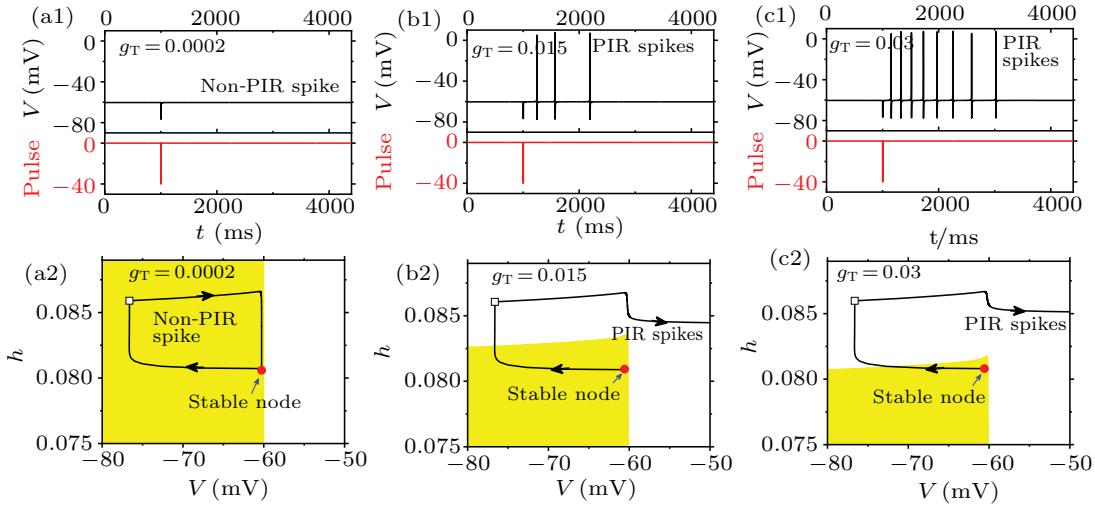


Fig. 6. The dynamics at bottom, middle, and top red arrows in Fig. 5. Upper row: Membrane potential (upper panel) and pulse stimulation (lower panel). (a1) Non-PIR spike at bottom red arrow for $g_T = 0.0002$ μS/cm² and $I = 1.145$ μA/cm²; (b1) PIR spike at middle red arrow for $g_T = 0.015$ μS/cm² and $I = 1.134$ μA/cm²; (c1) PIR spike at top red arrow for $g_T = 0.03$ μS/cm² and $I = 1.123$ μA/cm². Lower row: The threshold curve (i.e., border between blank and yellow regions) for non-PIR spike and PIR spikes in upper row. The color codes for yellow and blank areas please refer to Fig. 2. The pulse strength is -40 μA/cm² and width is 5 ms.

The dynamics at bottom, middle, and top red arrows in Fig. 5 are illustrated in Figs. 6(a1), 6(b1), and 6(c1), where g_T (conductance of T_{Ca} current) is 0.0002 μS/cm^2, 0.015 μS/cm^2, and 0.03 μS/cm^2, respectively. Upper panel represents the membrane potential (black) and lower panel denotes inhibitory stimulation (red). The initial resting state is set close to the SNIC bifurcation, respectively. Figures 6(b1) and 6(c1) show the PIR spikes appearing at larger g_T, while figure 6(a1) shows the non-PIR spike at smaller g_T. The larger the g_T is, the shorter latency of the first spike is, and the more the spikes are, as illustrated in Figs. 6(b1) and 6(c1). These results resemble experimental observations related to absence seizure and Parkinson diseases to a certain extent.[16,29,31,32]

Figures 6(a2), 6(b2), and 6(c2) provide threshold curves (i.e., border between blank and yellow regions) for the non-PIR spike and PIR spikes in Figs. 6(a1), 6(b1), and 6(c1), respectively. These threshold curves result from the projection of threshold surface onto plane (V, h), where n is fixed at the value of stable node (red solid circle). The square corresponds to the termination of the stimulation. For smaller g_T (Fig. 6(a2)), only "positive" threshold appears and thus the inhibitory stimulation-evoked phase trajectory (black) cannot run across threshold, i.e., forming non-PIR spike. For larger g_T (Figs. 6(b2) and 6(c2)), the "negative" threshold appears and suitable inhibitory stimulation can push neuronal state beyond such threshold to form PIR spikes. Moreover, the larger the g_T is, the closer the stable node to the "negative" threshold is, as depicted in Figs. 6(b2) and 6(c2), which implies the easier the generation of PIR spikes is. In short, the increase of T_{Ca} current brings the neuronal state closer to SNHO$_B$. The closer the neuronal state to SNHO$_B$ is, the easier the neuron to elicit PIR spikes is. The shape of "negative" threshold curve here is different from those of Figs. 2 and 3 in (V, n) plane, due to threshold curve here is projection of threshold surface onto plane (V, h).

3.5. The relationship between SNHO$_B$ and PIR phenomenon in thalamic model

3.5.1. SNHO$_B$ bifurcation and PIR spikes

Shown in Fig. 7 are the bifurcations in two-parameter plane (I, g_T) in the thalamic model. Such a thalamic model not only identifies the role of SNHO$_B$ in the PIR phenomenon, but also can be used to simulate the PIR spike observed in thalamic neurons in the experiments related to absence seizure and Parkinson disease. The SNIC (green) changes to BHom (black) via SNHO$_B$ (red star) as g_T is increased. PIR appears for the SNIC close to SNHO$_B$ while not for that far from SNHO$_B$, as indicated by the red arrows. The detailed dynamics of PIR spike or non-PIR spike are further depicted in Fig. 8. With increasing g_T, the inhibitory stimulation-induced neuronal response (black traces in upper panel) changes from non-PIR spike (Fig. 8(a)) at smaller $g_T = 0.002$ μS/cm^2 to PIR spikes (Figs. 8(b), 8(c)) at larger $g_T = 0.3$ μS/cm^2 and 0.6 μS/cm^2. The simulation results closely match those of the experimental results.[16,29,31,32,49]

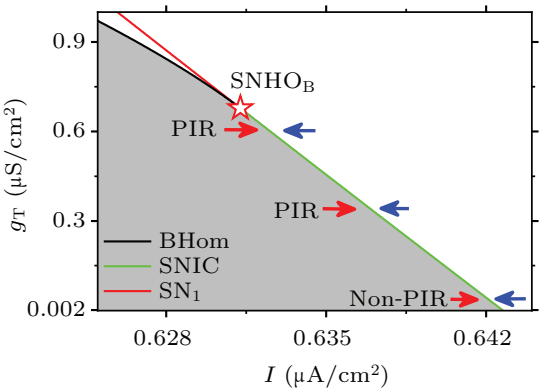


Fig. 7. The bifurcations related to PIR spike and non-PIR spike in two-parameter plane (I, g_T) in the thalamic model. The codes for plots and symbols and colors are same with those in Fig. 5. The detailed dynamics at red arrows are shown in Fig. 8 and at blue arrows are shown in Fig. 11.

3.5.2. The T_{Ca} current for PIR spikes

Moreover, the complex roles of T_{Ca} current (i.e., I_T) are shown in middle panels of Figs. 8(a)–8(c). For $g_T = 0.002$ μS/cm^2, the I_T is nearly zero before, during, and after the inhibitory stimulation, as depicted in middle panel of Fig. 8(a). Then, the behavior is still resting state and no PIR spike is induced. For $g_T = 0.3$ μS/cm^2, within the inhibitory stimulation, V decreases to a low level, which induces the positive I_T decreased at first and then increased, as illustrated in middle panel of Fig. 8(b). After the stimulation, the increased positive I_T enhances the membrane potential. Such enhanced membrane potential further activates the potassium channel to elicit a spike or action potential, i.e., a PIR spike. During such spike, the I_T further increases and then induces the following multiple spikes. Notably, during and after stimulation, I_T for $g_T = 0.6$ μS/cm^2 (Fig. 8(c)) is much stronger than those of $g_T = 0.3$ μS/cm^2 (Fig. 8(b)), which is the reason that more PIR spikes appear in Fig. 8(c) than those in Fig. 8(b).

As shown in middle panel of Figs. 8(b) and 8(c), T_{Ca} current $I_T = -g_T p_{T,\infty}^2(V) h_T (V - E_T)$ exhibits complex dynamics. I_T increases not only at low level V (at the ending part of the inhibitory stimulation) but also at high level V (during spike), which can be explained by the steady or active functions of activation gate

$$p_{T,\infty}(V) = \left(1 + \exp\left(\frac{-60 - V}{6.2}\right)\right)^{-1}$$

and inactivation gate

$$h_{T,\infty}(V) = \left(1 + \exp\left(\frac{84 + V}{4}\right)\right)^{-1},$$

as shown by blue curve and black curve in Fig. 9, respectively. The red dashed vertical line denotes the V value of the stable node. As V decreases, $h_{\mathrm{T},\infty}(V)$ increases while $p_{\mathrm{T},\infty}(V)$ decreases. At the ending part of inhibitory stimulation with a reduced V value, the increased h_{T} value related to large $h_{\mathrm{T},\infty}(V)$ is dominant, whereas decreased $p_{\mathrm{T},\infty}(V)$ plays a minor role, in enhancing I_{T}. As V increases, $h_{\mathrm{T},\infty}(V)$ decreases while $p_{\mathrm{T},\infty}(V)$ increases, as shown in Fig. 9. During a spike with high membrane potential V, the increased $p_{\mathrm{T},\infty}(V)$ is dominant while the decreased h_{T} due to small $h_{\mathrm{T},\infty}(V)$ plays a minor role, resulting in enhancing I_{T}. In a word, the complex cooperation between h_{T} and $p_{\mathrm{T},\infty}(V)$ determines the enhanced trend of I_{T} current regardless of whether the membrane potential is increased to high level or decreased to low level.

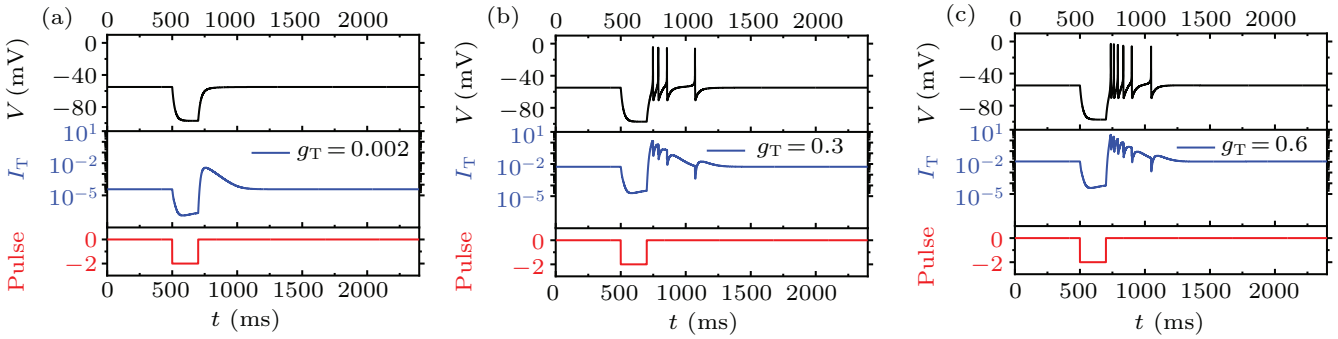


Fig. 8. The dynamics at red arrows shown in Fig. 7. (a) Non-PIR spike for the bottom red arrow: $g_{\mathrm{T}} = 0.002$ μS/cm^2 and $I = 0.641$ μA/cm^2; (b) PIR spikes for the middle red arrow: $g_{\mathrm{T}} = 0.03$ μS/cm^2 and $I = 0.636$ μA/cm^2; (c) PIR spike for the top red arrow: $g_{\mathrm{T}} = 0.6$ μS/cm^2 and $I = 0.631$ μA/cm^2. In each figure, top, middle, and bottom panels represent the membrane potential, T_{Ca} current, and pulse stimulation, respectively. The pulse strength is -2 μA/cm^2 and width is 200 ms.

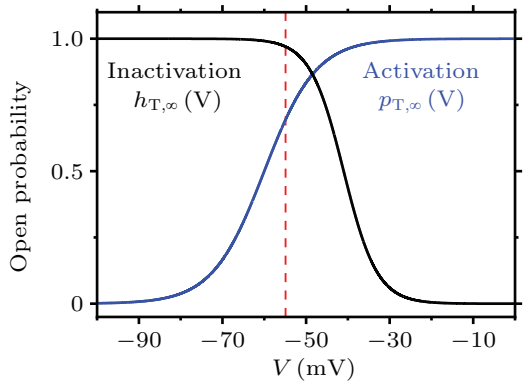


Fig. 9. Active function of activation gate $p_{\mathrm{T},\infty}(V) = \left(1+\exp\left(\frac{-60-V}{6.2}\right)\right)^{-1}$ and inactivation gate $h_{\mathrm{T},\infty}(V) = \left(1+\exp\left(\frac{84+V}{4}\right)\right)^{-1}$ of T_{Ca} channel. Red dashed line represents the membrane potential of the resting state.

3.5.3. "Positive" and "negative" threshold surfaces

The relationship between PIR spike and threshold surface in phase space (V, h_{Na}, h_{T}) is depicted in Fig. 10. For the non-PIR spike in Fig. 8(a) with small g_{T}, the phase trajectory is shown in Fig. 10(a1), and the threshold surface is vertical, as depicted by cyan in Fig. 10(a2) (local dynamics around stable node (red circle)). Phase trajectory initiating from the space left to the threshold surface results in subthreshold oscillations and right to the surface results in spike. The threshold surface locates right to the stable node (red circle) and exhibits V values lager than the stable node, i.e., a "positive" threshold. During the inhibitory stimulation (prior to the red hollow square which represents the termination of stimulation), V decreases and phase trajectory cannot run across the "positive" threshold surface. Then, phase trajectory after the inhibitory stimulation (following the red hollow square) results in non-PIR spike (subthreshold oscillation), as shown in Fig. 10(a2).

For the PIR spikes in Fig. 8(c) with large g_{T}, phase trajectory is shown in Fig. 10(b1), and the threshold surface is approximately horizontal with a maximal value, as shown by pink in Fig. 10(b2) (local dynamics around stable node (red circle)). The right part of threshold surface exhibits V values larger than the stable node, whereas the left part manifests V values lower than the stable node, i.e., a "negative" threshold. Phase trajectory initiating from the space lower to the threshold surface (in h_{Na} direction) results in subthreshold oscillations and upper to the surface results in spike. During the inhibitory stimulation, V decreases and phase trajectory runs across the left part ("negative") of the threshold surface into upper space (in h_{Na} direction), resulting in PIR spike after the inhibitory stimulation (Figs. 10(b1) and 10(b2)).

Figure 10(c) illustrates the comparison of the threshold surface between small and large g_{T}. The space left to the cyan threshold surface and above the pink cyan threshold surface should be emphasized. Such a space denotes the subthreshold region (phase trajectory initiating from which forms subthreshold oscillation instead of spike) for small g_{T}, while denotes spike region (phase trajectory initiating from which forms spike instead of subthreshold oscillation) for large g_{T}. The left part of cyan threshold surface exhibits V values lower than that of the stable node, corresponding to the negative threshold and PIR spike.

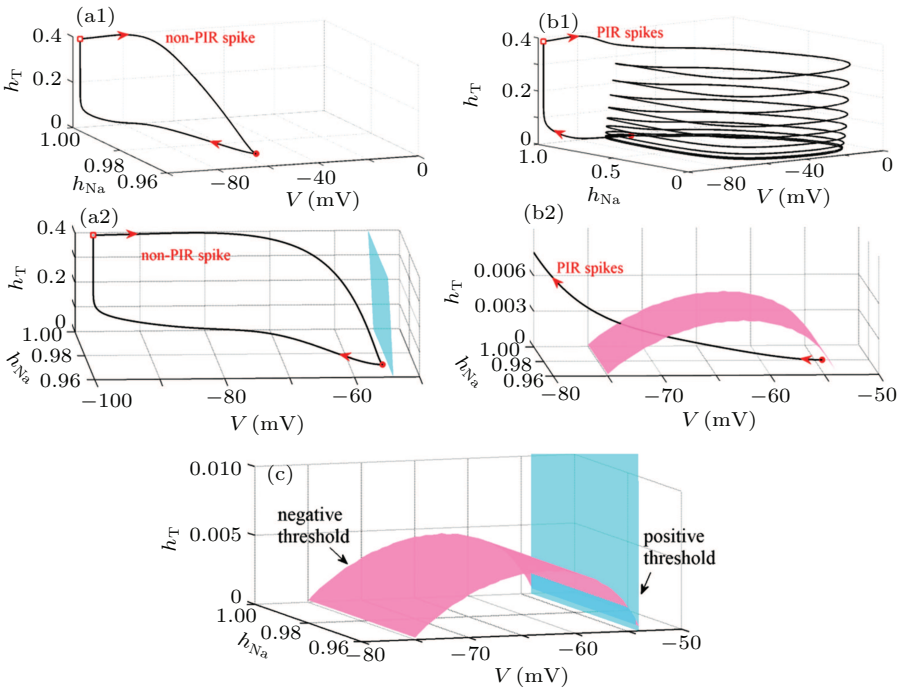


Fig. 10. The relationship between threshold surface and phase trajectory. Non-PIR spike in Fig. 8(a) with small g_T and PIR spikes in Fig. 8(c) with large g_T. (a1) The phase trajectory for non-PIR spike. (a2) The threshold surface (cyan) for non-PIR spike. (b1) The phase trajectory for PIR spikes. (b2) The threshold surface (pink) for PIR spikes. (c) The superposition of two threshold surfaces in panels (a2) and (b2).

3.5.4. PIR spiking

In addition, for a spiking, the inhibitory stimulation can suppress the spiking to be silent phase at first and then PIR spiking (continuous spikes with much higher frequency) appears after the stimulation, which are similar to the experimental observations[30] and related to absence seizure.[29,32] In the present paper, the enhanced PIR spiking can be simulated for the spiking behavior close to $SNHO_B$ and at large g_T, as shown in Figs. 11(b) and 11(c) (corresponding to middle and top blue arrows in Fig. 7), while the PIR spiking is not enhanced for the spiking far from the $SNHO_B$ and at small g_T (corresponding to bottom blue arrow in Fig. 7), as shown in Fig. 11(a). The T_{Ca} current for PIR spiking are depicted in the middle panel of Figs. 11(b) and 11(c), similar to those of PIR spikes (middle panel of Figs. 8(b) and 8(c)).

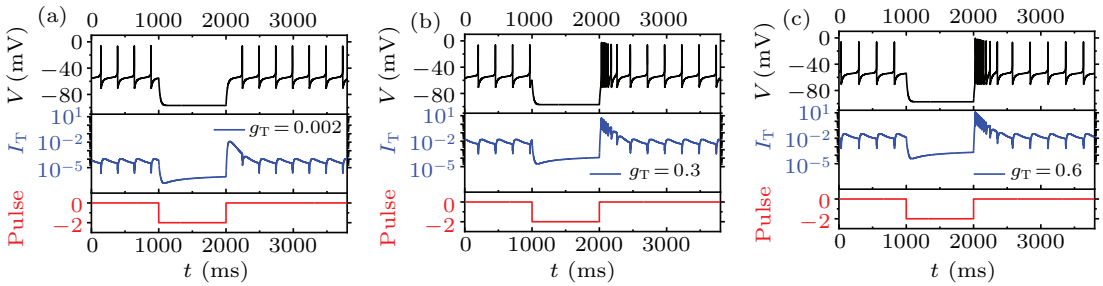


Fig. 11. The dynamics at three blue arrows in Fig. 7. (a) Non-PIR spiking for the bottom blue arrow: $g_T = 0.002$ μS/cm^2 and $I = 0.66$ μA/cm^2; (b) PIR spiking for the middle blue arrow: $g_T = 0.03$ μS/cm^2 and $I = 0.65$ μA/cm^2; (c) PIR spiking for the top blue arrow: $g_T = 0.6$ μS/cm^2 and $I = 0.64$ μA/cm^2. In each figure, top, middle, and bottom rows represent the membrane potential, T_{Ca} current, and pulse stimulation, respectively. The pulse strength is -2 μA/cm^2 and width is 1000 ms.

3.5.5. Comparisons to enhanced firing induced by excitatory modulation

In the present paper, the counterintuitive post-inhibitory rebound spike related to seizure and Parkinson diseases are the focus. To present comprehensive view of the enhanced firing related to seizure, the enhanced firing activity induced by excitatory stimulation is presented, as shown in Fig. 12, where the SNIC bifurcation corresponds to that at the middle arrow in Fig. 7. For the resting state near such SNIC, excitatory pulse stimulation (lower panel, red) with suitable strength can induce firing activity (upper panel, black), as shown in Figs. 12(a1), 12(a2), and 12(a3). In addition, static positive or depolarization modulation such as increase of background current I can induce enhancement of firing activity, as shown in Fig. 12(b) and insets therein. These enhanced firing activities induced by excitatory modulation, and these suppressed firing activities induced by inhibitory modulation, are the common phenomena related to seizures and not the focus of the present paper.

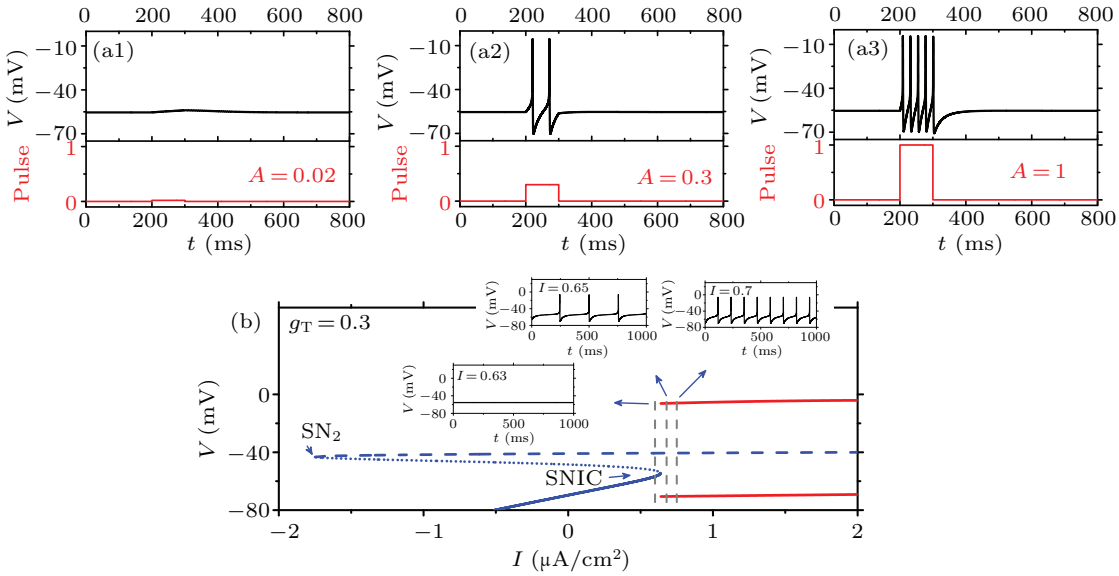


Fig. 12. The firing activity induced by excitatory stimulation and background current I. Top row: the response of resting neuron to excitatory stimulation is enhanced with increasing pulse strength A: $g_{\rm T} = 0.3$ μS/cm^2 and $I = 0.63$ μA/cm^2. The pulse width is fixed at 100 ms. Bottom row: The SNIC bifurcation (right knee of the S-shape curve) corresponds to that at the middle arrow in Fig. 7 at $g_{\rm T} = 0.3$ μS/cm^2. The neuronal firing activity is enhanced with increasing background current I from 0.63 μA/cm^2 (left vertical line), to 0.65 μA/cm^2 (middle vertical line), 0.7 μA/cm^2 (right vertical line). The details for bifurcation diagram please refer to Fig. 2.

4. Conclusions and perspectives

PIR spike, which is induced by inhibitory modulation, is closely linked to important nonlinear concepts such as threshold and bifurcations. This phenomenon is also associated with various brain functions and diseases, including absence seizure and Parkinson diseases.[16,26–32] Therefore, understanding how to modulate the PIR spike is crucial for both nonlinear physics and neuroscience. This paper investigates the PIR spike and its relationship to threshold and bifurcations (codimension-1 and -2) by modulating multiple parameters, including the T-type Ca^{2+} channel, in various models. The results exhibit significances in the following aspects.

Firstly, our study uncovers a universal codimension-2 bifurcation mechanism for the PIR spike. Such a bifurcation called saddle-node homoclinic orbit ($\rm SNHO_B$) is identified in 4 neuronal models especially including the thalamic model. Moreover, multiple parameters can be modulated to induce the appearance of $\rm SNHO_B$. Our study finds that PIR spike does not appear for the SNIC far from the $\rm SNHO_B$, but for the SNIC close to the $\rm SNHO_B$. Such a result extends the codimension-1 bifurcations for PIR spike from Hopf and BHom in the previous studies[1,18] to SNIC. Additionally, it reveals a new border between non-PIR spike and PIR spike, which occurs at a certain SNIC bifurcation close to $\rm SNHO_B$. Previous studies have suggested that such border is BT due to the PIR spike for Hopf bifurcation.[48,49] Therefore, our results present codimension-2 bifurcation underlying PIR spike, provide comprehensive recognitions between PIR spike and bifurcations, bring novel viewpoint for the transition between non-PIR spike and PIR spike.

Secondly, $\rm SNHO_B$ provides a dynamical interpretation to the seemingly contradictory result of SNIC for non-PIR spike in the ML model[1] and PIR spike in the $I_{\rm Na,p} + I_{\rm K}$ model.[47] By changing slope of n-nullcline, the SNIC for non-PIR spike in the ML model is identified to be far from the $\rm SNHO_B$, while that for PIR spike in the $I_{\rm Na,p} + I_{\rm K}$ model is close to the $\rm SNHO_B$. The increase of slope of n-nullcline induces the SNIC bifurcation to be close to the $\rm SNHO_B$, which is the essential reason for the appearance of PIR spike for both models. Then, the modulation to the slope of the n-nullcline presents a feasible measure to modulate the PIR spike.

Finally, the $\rm SNHO_B$ that underlies the PIR phenomena mediated by $T_{\rm Ca}$ channel provides a dynamic interpretation for experimental observations[16,26,29–32] of the absence seizure and Parkinson diseases induced by inhibitory stimulation. By increasing the conductance of the $T_{\rm Ca}$ channel, which modulates SNIC to be closer to the $\rm SNHO_B$, the inhibition-induced $T_{\rm Ca}$ current becomes stronger, leading to the appearance of PIR spikes or PIR spiking. Such enhancement of neuronal behavior induced by inhibition has been identified as a factor in the pathogenesis of absence seizure and Parkinson diseases. To relieve seizure or Parkinson diseases by inhibiting pyramidal neurons, a crucial step is to avoid the PIR phenomena. This can be achieved, for example, by modulating the behavior of pyramidal neurons to be SNIC far from the $\rm SNHO_B$ through decreasing the conductance of $T_{\rm Ca}$ current. In addition, the complex evolution process of $T_{\rm Ca}$ current in the generation of PIR phenomenon is obtained. These results provide not only bifurcation mechanism for pathogenesis of seizure or Parkinson diseases, but also new perspective on treatment options.

In the future, further studies on PIR spike should be conducted in the following areas. Firstly, theoretical explanations

for PIR spike and additional factors that modulate PIR spike should be provided. Secondly, dynamical mechanisms for PIR spike should be investigated in more neuronal and network models to explore brain functions or diseases, by modulating other factors such as synapse. Finally, a comparison between PIR spike mediated by the T_{Ca} channel and hyperpolarization-activated cation current (Ih) should be conducted. This will provide a deeper understanding of the similarities and differences between the two mechanisms and their respective roles in brain function and diseases.

Appendix A

Three figures are provided to represent the SHom and BHom orbit bifurcations shown in Fig. 4(a1), equilibrium point and phase trajectory, and PIR spike or not in the ML model, respectively.

Figure A1 represents the SHom and BHom bifurcations at $V_4 = 7.3$ mV (Fig. A1(a)) and $V_4 = 23$ mV (Fig. A1(b)) in the ML model, respectively. Except for SHom or BHom, the SN_1 and SN_3 denote saddle-node bifurcation of equilibrium point, which correspond to the bifurcation curves of SN_1 and SN_3 in Fig. 4(a1). The difference of SHom and BHom can be well interpreted from their phase trajectories, which are depicted in Fig. A2.

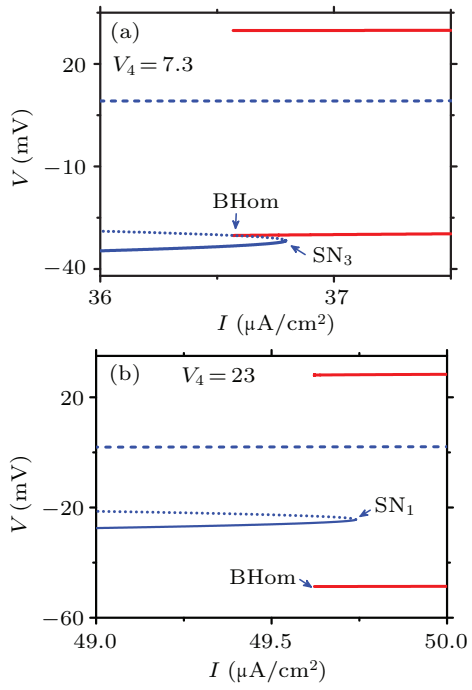


Fig. A1. The homoclinic orbit bifurcations in the ML model. SHom and BHom denote the small and big homoclinic orbit bifurcation, respectively. SN_1 and SN_3 represent saddle-node bifurcation of equilibrium point. The details for other plots please refer to Fig. 2. (a) $V_4 = 7.3$ mV and SHom occurs at about $I = 36.5683$ μA/cm^2; (b) $V_4 = 23$ mV and BHom occurs at about $I = 49.62212$ μA/cm^2.

Shown in Fig. A2(a) is the phase trajectory for SHom orbit and in Fig. A2(b) the one for BHom orbit. These two trajectories both begin from and end at the saddle (half-filled circle) and run in anti-clockwise. Such closed orbit is the homoclinic orbit. The BHom orbit is big, which contains the stable node (red solid circle), as illustrated in Fig. A2(b) (the insert figure is enlargement around the node and saddle).

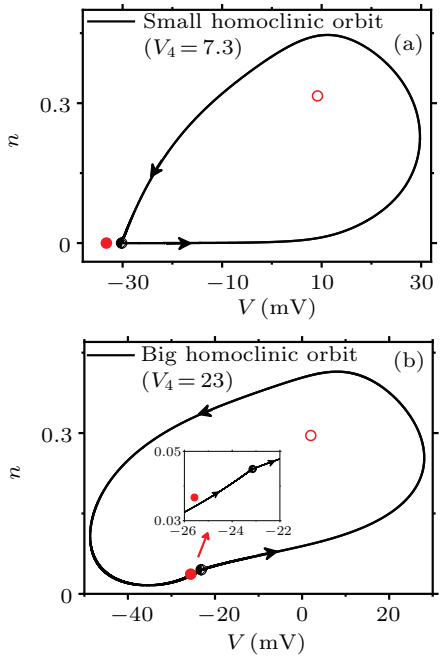


Fig. A2. The homoclinic orbit (black curve) and the stable node (red solid circle), saddle (half-filled circle), and unstable focus (hollow red circle). (a) SHom orbit in Fig. A1(a); (b) BHom orbit in Fig. A1(b). Inset shows the details around the saddle and stable equilibrium points.

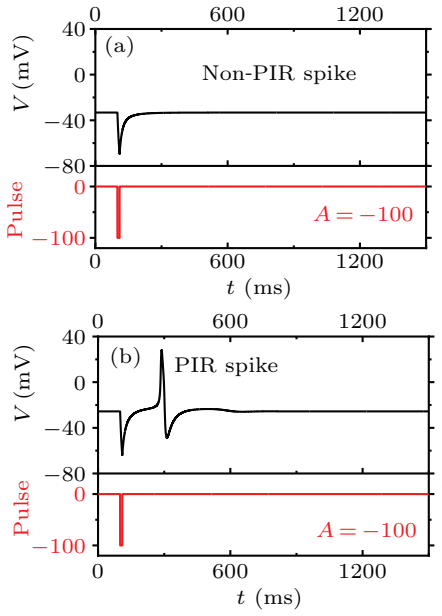


Fig. A3. The inhibitory stimulation-induced responses (black, upper panel) initiating from the resting state close to homoclinic orbit bifurcations in Fig. A1. Lower panel represents the inhibitory stimulation (red) (strength $A = -100$ μA/cm^2 and pulse width 10 ms). (a) Non-PIR spike induced from resting state at $V_4 = 7.3$ mV and $I = 36.568$ μA/cm^2 (close to SHom bifurcation in Fig. A1(a)); (b) PIR spike induced from resting state is set at $V_4 = 23$ mV and $I = 49.620$ μA/cm^2 (close to BHom bifurcation in Fig. A1(b)).

In addition, the unstable focus (hollow red circle) is within the BHom orbit. However, SHom orbit (Fig. A2(a))

is small, and the stable node locates outside. From the geometrical characteristics, the BHom is favorable for PIR spike whereas the SHom not. As expected, for BHom bifurcation, PIR spike is induced, as illustrated in Fig. A3(b), and the non-PIR spike appears for SHom bifurcation, as illustrated in Fig. A3(a). The lower panel represents the inhibitory stimulation (red) and the upper panel denotes the membrane potential (black). More details about the PIR for BHom please refer to Ref. [18]. The SHom bifurcation here is close to the $SNHO_S$ in Fig. 4(a1). The non-PIR spike for such SHom implies that $SNHO_S$ does not have the role to guarantee the PIR spike in ML model.

Acknowledgements

Project supported by the National Natural Science Foundation of China (Grant Nos. 12072236, 11872276, and 11802086), the Postdoctoral Research Project of Henan Province, China (Grant No. 19030095), and the Science and Technology Development Program of Henan Province, China (Grant No. 212102210543).

References

[1] Izhikevich E M 2000 *Int. J. Bifurcation Chaos* **10** 1171
[2] Yan B, Panahi S, He S, *et al*. 2020 *Nonlinear Dyn.* **101** 521
[3] Yilmaz E, Ozer M, Baysal V, *et al*. 2020 *Sci. Rep.* **6** 30914
[4] Ma J 2023 *J. Zhejiang Univ. Sci. A* **24** 109
[5] Cao B, Gu H G and Li Y Y 2021 *Chin. Phys. B* **30** 050502
[6] Liu Y R and Liu S Q 2020 *Nonlinear Dyn.* **101** 531
[7] Wang J J, Yang Y, Gao Z W, *et al*. 2020 *Chin. Phys. B* **29** 058701
[8] Xu Y, Liu M H, Zhu Z G and Ma J 2020 *Chin. Phys. B* **29** 98704
[9] Valenti O, Cifelli P, Gill K M, *et al*. 2011 *J. Neurosci.* **31** 12330
[10] Badimon A, Strasburger H J, Ayata P, *et al*. 2020 *Nature* **586** 417
[11] Hesse J, Schleimer J H, Maier N, *et al*. 2022 *Nat. Commun.* **13** 3934
[12] Tang X, Jaenisch R and Sur M 2021 *Nat. Rev. Neurosci.* **22** 290
[13] Arinyo-I-Prats A, Moreno-Spiegelberg P, Matias M A, *et al*. 2021 *Phys. Rev. E* **104** L052203
[14] Fan D G, Zheng Y H, Yang Z C, *et al*. 2020 *Appl. Math. Mech. Engl. Ed.* **41** 1287
[15] Du M M, Li J J, Chen L, *et al*. 2018 *PLoS Comput. Biol.* **14** e1005877
[16] Kim J, Kim Y, Nakajima R, *et al*. 2017 *Neuron* **95** 1181
[17] Park C, Rubchinsky L L and Ahn R 2021 *Chaos* **31** 113121
[18] Wang X J, Gu H G and Lu B 2021 *ERA* **29** 2987
[19] Li L, Zhao Z G and Gu H G 2022 *Chin. Phys. B* **31** 070506
[20] Lu A C, Lee C K, Kleiman-Weiner M, *et al*. 2020 *eLife* **9** e59548
[21] Ferrante M, Shay C F, Tsuno Y, *et al*. 2017 *Cerebral Cortex* **27** 2111
[22] Guan L N, Jia B and Gu H G 2019 *Internat. J. Bifur. Chaos* **29** 1950198
[23] Goaillard J, Taylor A, Pulver S, *et al*. 2010 *J. Neurosci.* **30** 4687
[24] Felix A, Fridberger A, Leijon S, *et al*. 2011 *J. Neurosci.* **31** 12566
[25] Villalobos C A and Basso M A 2022 *Cell Reports* **39** 110699
[26] Nejad M M, Rotter S and Schmidt R 2021 *Eur. J. Neurosci.* **54** 4295
[27] Yang Y, Cui Y, Sang K, *et al*. 2018 *Nature* **554** 317
[28] Howe W M and Kenny P J 2018 *Nature* **554** 304
[29] Kim D, Song I, Keum S, *et al*. 2001 *Neuron* **31** 35
[30] Sessolo M, IMarcon I, Bovetti S, *et al*. 2015 *J. Neurosci.* **35** 9544
[31] Chang M, Dian J A, Dufour S, *et al*. 2018 *Neurobiology of Disease* **109** 102
[32] Cheong E, Zheng Y, Lee K, *et al*. 2009 *PNAS* **106** 21912
[33] Ellender T J, Raimondo J V, Irkle A, *et al*. 2014 *J. Neurosci.* **34** 15208
[34] de Curtis M and Avanzini G 2001 *Prog. Neurobiol.* **63** 541
[35] Cammarota M, Losi G, Chiavegato A, *et al*. 2013 *J. Physiol.* **591** 807
[36] Schevon C, Weiss S, McKhann G, *et al*. 2012 *Nat Commun.* **3** 1060
[37] Ledri M, Madsen M G, Nikitidou L, *et al*. 2014 *J. Neurosci.* **34** 3364
[38] Zhao J Y, Yu Y and Wang Q Y 2022 *Chaos, Solitons and Fractals* **164** 112720
[39] Tikidji-Hamburyan R A, Martinez J J, White J A, *et al*. 2015 *J. Neurosci.* **35** 15262
[40] Li Y Y, Gu H G, Jia B, *et al*. 2021 *Sci. China Technol. Sci.* **64** 1459
[41] Lu B, Gu H G, Wang X J, *et al*. 2021 *Chaos, Solitons and Fractals* **145** 110817
[42] Yang Y X, Gu H G, Li Y Y, *et al*. 2023 *Nonlinear Dyn.* **111** 7751
[43] Wu F Q, Gu H G and Li Y Y 2019 *Commun. Nonlinear Sci. Numer. Simul.* **79** 104924
[44] Yao C G, He Z W, Nakano T, *et al*. 2019 *Nonlinear Dyn.* **97** 1425
[45] Ding X L, Jia B and Li Y Y 2019 *Acta Phys. Sin.* **68** 180502 (in Chinese)
[46] Wang X J and Gu H G 2022 *ERA* **30** 459
[47] Wang X J, Gu H G, Li Y Y, *et al*. 2022 *Mod. Phys. Lett. B* **36** 2250082
[48] Zeberg H, Blomberg C and Arhem P 2010 *PLoS Comput. Biol.* **6** e1000753
[49] Liu C M, Liu X L and Liu S Q 2014 *Biol. Cybern.* **108** 75
[50] Nigam A, Hargus N J, Barker B S, *et al*. 2019 *Epilepsy Res.* **154** 132
[51] Stephenson-Jones M, Yu K, Ahrens S, *et al*. 2016 *Nature* **539** 289
[52] McGregor M M and Nelson A B 2001 *Neuron* **101** 1042
[53] Wang Z H and Duan L X 2022 *Nonlinear Dyn.* **108** 191
[54] Njap F, Claussen J C, Moser A, *et al*. 2012 *Cogn. Neurodynamics* **6** 333
[55] Gerstner W, Kistler W M, Naud R, *et al*. 2014 *Neuronal Dynamics: From Single Neurons to Networks and Models of Cognition* (Cambridge University Press)
[56] Zhu T, Wei S and Wang Y 2022 *J. Pain Res.* **15** 2029
[57] Morris C and Lecar H 1981 *J. Biophys.* **35** 193
[58] Rinzel J, Terman D, Wang X J, *et al*. 1998 *Science* **279** 1351
[59] Rubin J E and Terman D 2004 *J. Comput. Neuronsci.* **16** 211
[60] Dhooge A, Govaerts W and Kuznetsov Y A 2003 *ACM Trans. Math Softw* **29** 141
[61] Ermentrout B 2002 *Simulating, analyzing, and animating dynamical systems: a guide to XPPAUT for researchers and students* (Philadelphia: SIAM Press)